Experimental and Numerical Seismic Evaluation of RC Walls Under Axial Compression

Tahir Mehmood[1], Ahsen Maqsoom[1], Adnan Nawaz[1*], Badar-Ul Ali Zeeshan[1]

[1] Department of Civil Engineering, COMSATS University Islamabad, Wah Campus, GT Road, Quaid Avenue, COMSATS University, Wah Cantt, Pakistan
* Corresponding author, e-mail: adnan.nawaz@ciitwah.edu.pk

Abstract

Recent studies show that code-based equations usually do not provide an accurate estimate for the shear strength of short reinforced concrete (RC) walls due to the negligence of many important factors including the beneficial effect of axial compression. In the current study, quasi-static reversed cyclic testing is conducted for two RC wall specimens, one under axial load and one without axial load to assess the effect of the axial compression on the shear strength of RC walls in high-rise buildings. The results of the experimental study show that the axial compression load significantly improves the shear strength of RC walls. Results are also compared with the performance-based seismic evaluation code practices. Based on the experimental findings, recommendations are made for improvements in the existing codes. The experimental results are further compared with different numerical models to explore the suitable computer modeling options for non-linear response prediction of RC walls.

Keywords

short RC walls, shear strength, axial compression, quasi-static

1 Introduction

In recent years, a noticeable increase of high-rise construction has been observed in major metropolitan cities around the world. RC walls, in combination with the moment resistant frame, are considered as an efficient lateral load resisting system. Flexural considerations dictate the design of RC walls in such high-rise buildings as their aspect ratio is more than 4. Seismic response of the high-rise RC wall structures is quite complex as numerous vibration modes, apart from the fundamental mode, significantly contribute to the response; called as "higher modes effects". Higher-modes effect can result in significant dynamic shear amplification at the base and the mid-height of RC walls, which can exceed the shear demand prescribed by the design codes [1–4]. Higher modes effect can also significantly lower down the resultant of lateral forces under extreme ground shakings [5, 6]. In such scenarios, the RC walls with aspect ratio more than 4, may fail prematurely in non-ductile shear mode instead of flexural-mode. Hence, the shear strength of such walls should also be checked by considering squat-wall-behavior.

ACI 318-11 [7] provides two approaches to evaluate the shear capacity of the RC walls; one approach has been given in Chapter 11, whereas, the second is prescribed in Chapter 21 of ACI 318-11. The Eq. (7) in Chapter 21 of ACI 318-11 [7] has remained mostly unchanged since 1983 [8]; this equation does not include the influence of axial load on the shear strength. The approach in the Section 11.9 of ACI 318-11 [7] reflects the influence of axial loading on shear strength, but still greatly underestimates the true shear strength of the RC walls [9, 10]. Apart from ACI-318 [7], other building codes, such as ASCE 43-05 [11], consider the effect of axial load on the shear strength of RC walls but still underpredict the shear strength for many of the test specimens [9].

Moreover, several researchers, such as Gulec et al. [9] and Bentz et al. [10], have established that the code-based empirical equations significantly underestimate the true shear strength of the shear-dominated RC wall, particularly under the effect of an axial load. This underestimation of the shear strength forces structural engineers to use high amounts of shear reinforcement, and in some cases, it even requires an increase in the size of the RC wall to achieve the desired level of shear strength. The conservative code-based equations may be suitable for the purpose

of design, but the evaluation of existing buildings requires a more rational approach for an economical retrofitting strategy. Structural engineers typically follow the performance-based seismic evaluation code to assess the deformation level corresponding to specific damage level, e.g., life safety (LS), collapse prevention (CP) etc. Guidelines in the current performance based seismic evaluation codes, such as ASCE-41-06 [12] and FEMA-356-2000 [13], are based on the limited data of experimental results especially for shear dominated RC walls. Therefore, it is required to conduct further research in this area to improve the understanding of the non-linear response of such RC shear walls, especially under high axial load.

The current case study focuses on the experimental and numerical investigation of shear dominated RC walls to determine the effect of high ratio axial load on the shear strength. The experimental program includes the quasi-static reversed cyclic lab testing of two shear dominated RC wall specimens. Both of the short specimens were identical in terms of dimensions and reinforcement, but one specimen was tested with an axial load applied at the top, and one specimen was tested without any axial load, to assess the influence of axial load on the shear strength of RC walls. Experimental outcomes were compared with the current performance-based seismic evaluation codes, ASCE-41-06 [12] and FEMA-356-2000 [13]. The results of the experimental study were also compared with the Finite Element (FE) model based on the modified compression field theory (MCFT) [14], which can consider the coupling of axial, flexure and shear responses. Contrary to the traditional uni-axial fiber model, the MCFT theory considers the reinforced concrete under biaxial loading conditions.

2 Experimental observations and comparison with design codes
The experimental program was comprised of two short RC wall specimens (SW1 and SW2). The aspect ratio of both specimens was kept at 0.7. A reversed cyclic quasi-static loading test was conducted for seismic performance evaluation. The specimen SW1 was tested under a constant axial load of 300 kN i.e., approximately 0.10 axial load ratio, whereas the specimen SW2 was tested without any axial load. The axial compression is generally normalized by compressive strength of concrete (fc') and the sectional area of RC wall (A) expressed as: $AR = P / Af_c'$, where AR is axial load ratio and P is axial compression load.

2.1 Specimen description
The geometry and reinforcement details of the specimens are presented in Fig. 1 where all dimensions are in millimeters (mm). For the longitudinal reinforcement (i.e., DB12 and DB10), Grade 60 steel was used, whereas for horizontal reinforcement (i.e., RB6), and confinement of boundary zones, SR240 steel was used. Table 1 presents the vertical, horizontal, and confinement reinforcement ratios as well as the compressive strength of the concrete and the yield strength of the reinforcement for the web and boundary zones of the specimens. The aspect ratio and the reinforcement details of both specimens were selected in such a way to force the shear mode of failure. Moreover, enough boundary reinforcement was provided to avoid the flexure mode of failure.

2.2 Experimental set up
The experimental setup, as shown in Fig. 2, consists of a gravity load frame to apply a constant axial load during the test. The built-in rollers at the top of the frame, permit
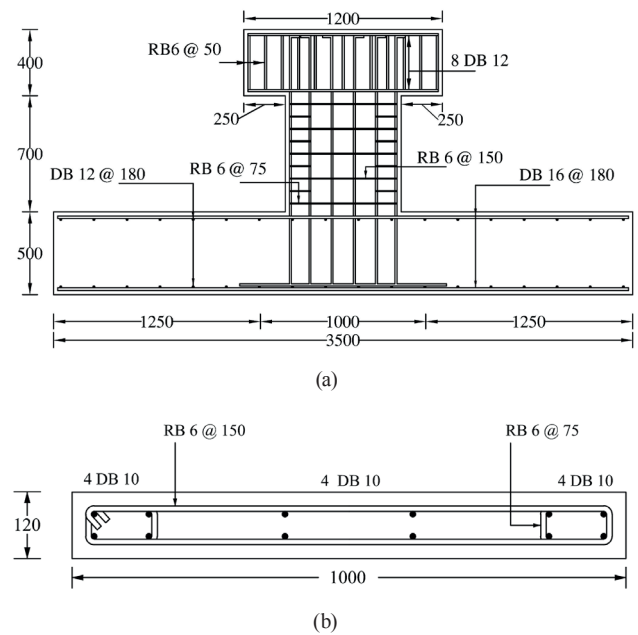

(a)

(b)

Fig. 1 (a) Dimensions and reinforcement details of the specimens (b) Cross-section of the specimens (all dimensions are in mm)

Table 1 Material Properties /reinforcement detail

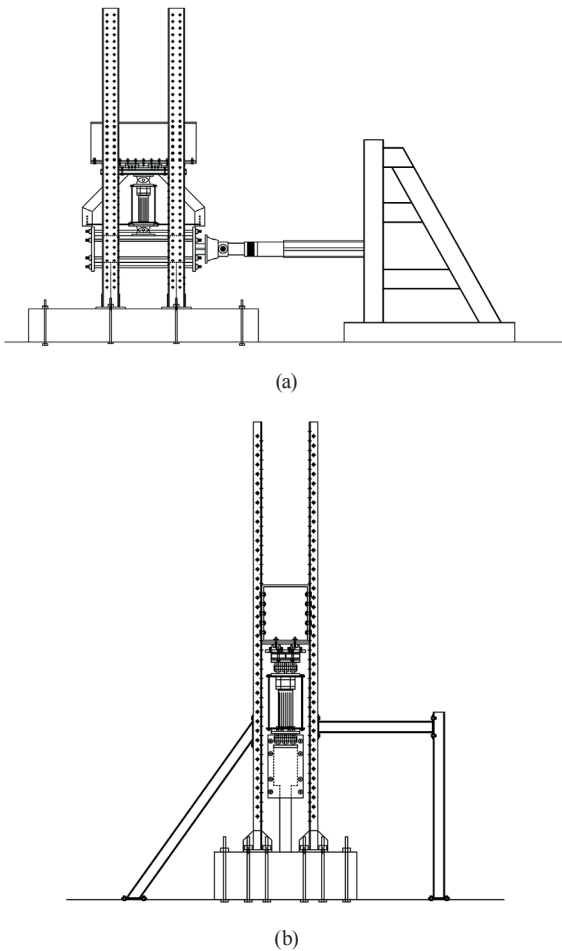| Zone	Concrete f_c' (Mpa)	Horizontal ρ(%)	f_y(Mpa)	Vertical ρ(%)	f_y(Mpa)	Confinement ρ(%)	f_y(Mpa)
Boundary	27	0.95	350	1.75	484	0.5	350
Web	27	0.34	350	0.37	484	-	-

(a)

(b)

Fig. 2 Experimental set up (a) Front view (b) Side view

the axial load to move along with the tip of the wall, hence simulating the actual conditions of the wall subjected to earthquake loading [15].

The specimen SW1 was subjected to a constant axial load of 300 kN (approximately 0.10 axial load ratio) using a 600 kN jack. The lateral load was applied using a 500 kN hydraulic actuator at the top of the specimen. The application of lateral load at the top of the wall gives a direct load path to the foundation, which might not be possible in tall walls with low shear-span ratio [16]; but, this loading scenario can simulate the behavior of long RC walls, subject to reversal in shear, below the level of ground due to the presence of stiff diaphragm and RC basement walls.

A quasi-static loading history was applied to the wall specimens, using a convenient target lateral drift. The percent lateral drifts of ±0.125, ±0.25, ±0.5, ±0.75, ±1.0, ±1.5, ±2.0, ±2.5, and ±3.0 were applied, until the specimens attained the gravity load-carrying capacity. In order to attain the hysteric behavior, two cycles of loading were employed with each drift ratio. Fig. 3 shows the loading protocol followed during the quasi-static testing of the specimens.

2.3 Instrumentation

Extensive instrumentation was employed to obtain valuable experimental data [17]. A total of forty strain gauges were installed to measure the reinforcement strain in the web and boundary regions of the specimens, as displayed in Fig. 4(a). Eighteen strain gauges were used to measure the strain in the longitudinal reinforcement; sixteen strain gauges were used to obtain the strain in the horizontal reinforcements, and six strain gauges were employed for confinement reinforcement in the boundary zones of the specimen. The lateral deformation of the shear wall, comprising of flexure, rigid body/rocking, shear, and sliding deformation, was measured using linear
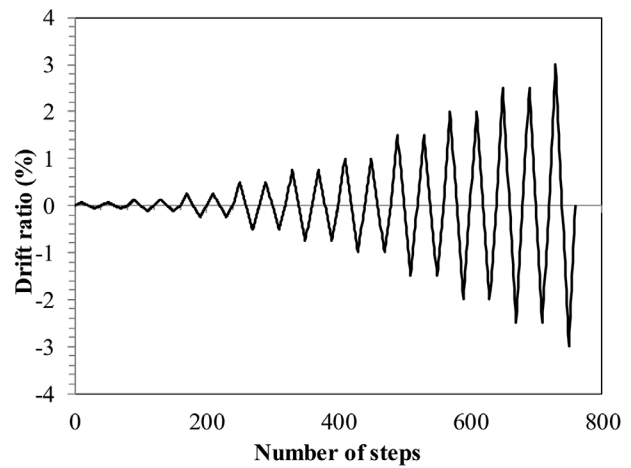

Fig. 3 Loading protocol for the reversed cyclic test
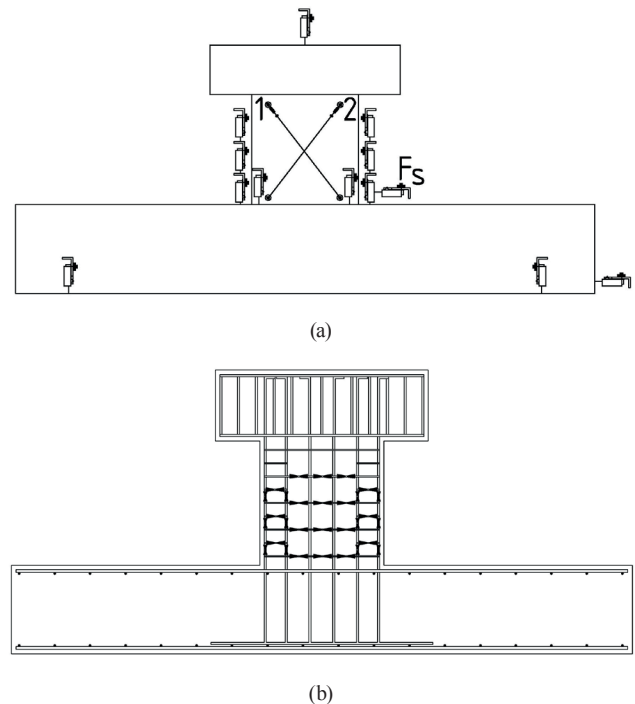

(a)

(b)

Fig. 4 (a) Strain gauge locations (b) LVDTs layout

variable differential transducers (LVDTs), as illustrated in Fig. 4(b). Three LVDTs were installed on both sides of the shear wall to measure the curvature distributions in the plastic hinge area, two LVDTs were used on the face of the shear wall to determine the rocking deformation of the shear wall, two LVDTs were installed in the form of "X" configuration to measure the shear deformations, whereas one LVDT (designated as F_s) was employed to measure the sliding deformation of the specimens, as illustrated in Fig. 4(b).

2.4 Summary of test results

The summary of test results is presented in Table 2, including lateral load and top displacement under both positive and negative loading at concrete cracking, yielding, peak loading, and at significant loss of lateral strength. Significant loss of lateral strength is defined as when the specimens were not able to take any axial load.

2.5 Damage propagation

In most of the previous studies, the experiments stopped at a 20 % drop in lateral strength, but in this study, the final failure was considered when the axial load capacity of a specimen was completely lost. The purpose of testing until the loss of the axial capacity was to develop the complete envelope of force-deformation, which is extremely important for performance-based design procedures. Therefore, the test continued until the axial load capacity was completely lost. A brief description of the crack propagation and the final failure mechanism is depicted here.

2.5.1 SW1 (10 % axial load compression)

Fig. 5 presents the crack development in the SW1 specimen with an increasing level of lateral drifts. Fig. 6 demonstrates the force-displacement relationship of the SW1 specimen. No visible cracking was observed at the drift levels of 0.125 % and 0.25 %. First, visible cracking was

Table 2 Summary of test results

Specimen ID	Loading direction	Cracking		Yielding		Peak Load		Strength Loss	
		F (kN)	Δ^{top} (mm)	F (kN)	Δ^{top} (mm)	F (kN)	Δ^{top} (mm)	F (kN)	Δ^{top} (mm)
SW1	Positive	274	4.4	335	6.6	377	12.2	146	17.8
	Negative	228	4.3	298	6.6	398	17.4	363	17.5
SW2	Positive	108	2.2	202	6.6	209	13.1	125	44
	Negative	113	2.2	196	6.6	235	13.2	122	44

(a) 0.25 % drift

(b) 0.5 % drift

(c) 0.75 % drift
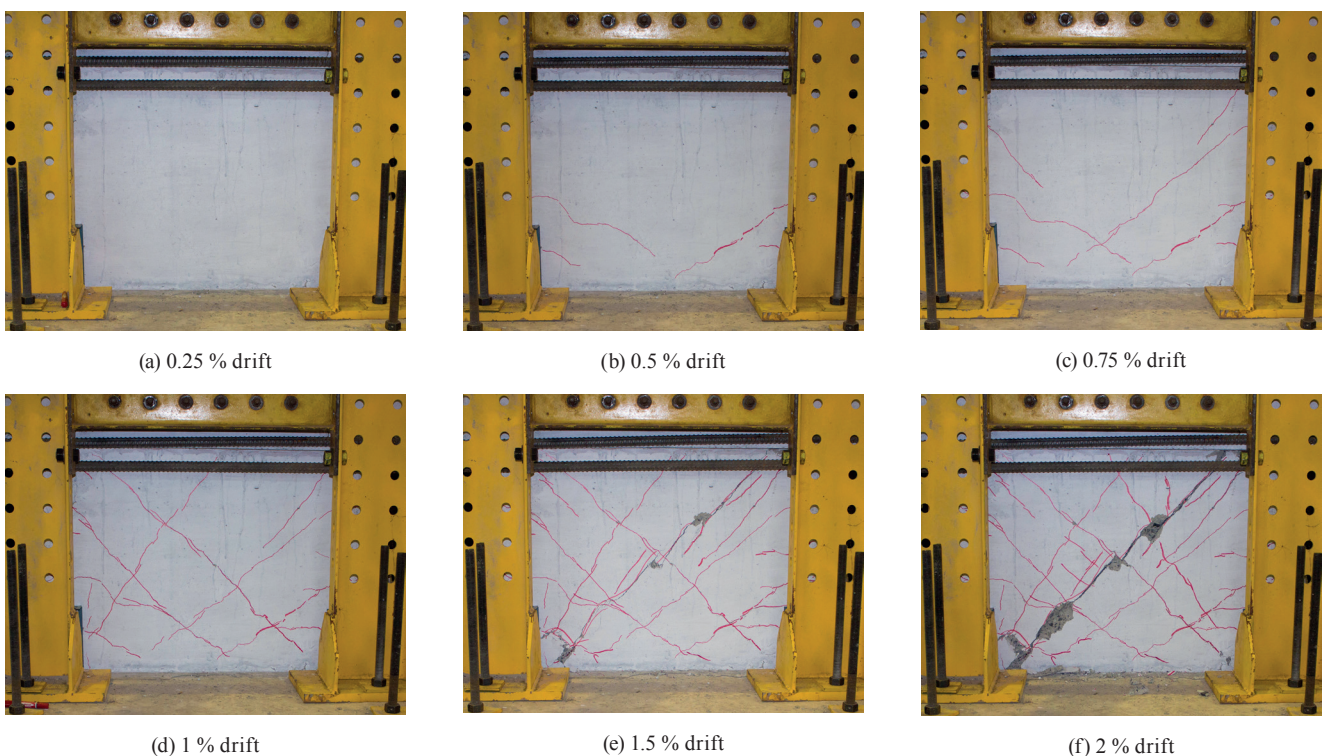
(d) 1 % drift

(e) 1.5 % drift

(f) 2 % drift

Fig. 5 Propagation of damage with drift increments specimen SW1
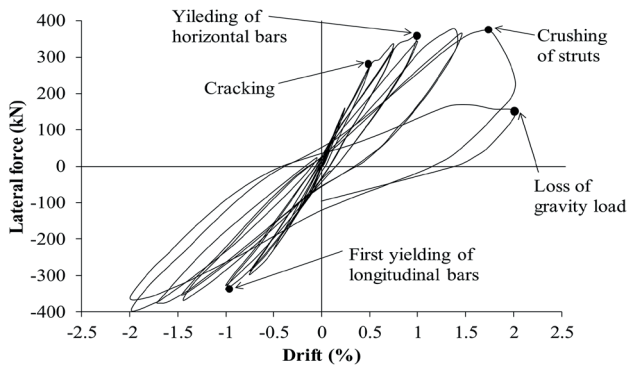
Fig. 6 Lateral force –drift relationship specimen SW1

noticed at the 1st cycle of −0.5 % drifts approximately at an angle of 35 degrees with the horizontal. The first yielding of the horizontal reinforcement was detected at the 2nd cycle of 0.75 % drift with significant inclined cracking. At this stage, few larger cracks appeared on the web. In the first cycle of 1 % drift, the longitudinal reinforcement also started yielding. The yielding of the longitudinal reinforcement immediately after the yielding of the horizontal reinforcement depicts the strong interaction of non-linear shear-flexure responses. At 1.5 % drift, severe cracking was noticed, with a visible spalling of the concrete. As a consequence of the axial load in the case of SW1 specimen, cracks were closed when the applied lateral drift reached the zero level during the unloading phase. With a

further increase of the lateral drift, an increase in cracks width was observed, but the RC specimen was able to sustain its peak shear strength until significant web crushing at 2 % drift. Finally, in the 2nd cycle of the 2 % drift, test was stopped when the specimen SW1 was not able to carry the applied axial load. A peak shear stress of $0.64\sqrt{f_c'}$ was observed, which is lower than the ACI 318-11 [7] limit of $0.83\sqrt{f_c'}$ to avoid diagonal compression failure. The failure mode of the SW1 specimen can be characterized as a diagonal tension failure.

2.5.2 SW2 (0 % axial load compression)

Fig. 7 presents the crack pattern observed in the specimen SW2, and the lateral drift-force relationship is presented in Fig. 8. First visible cracking was observed at 0.25 % drift. It should be noted that the first cracking in the SW1 specimen was detected at 0.5 % drift. The delayed cracking in the case of the SW1 specimen was due to the high cracking shear stress under the effect of axial compression. With further increase in the lateral drift, the width of the main diagonal crack increased. At 0.75 % drift, yielding in the longitudinal and the horizontal reinforcement was observed. At 1 % drift, the peak shear strength was reached. Lateral strength degradation started at 2 % drift with a ductility factor of approximately 4. A few more cracks appeared with an increase of the lateral drift, but the width of the
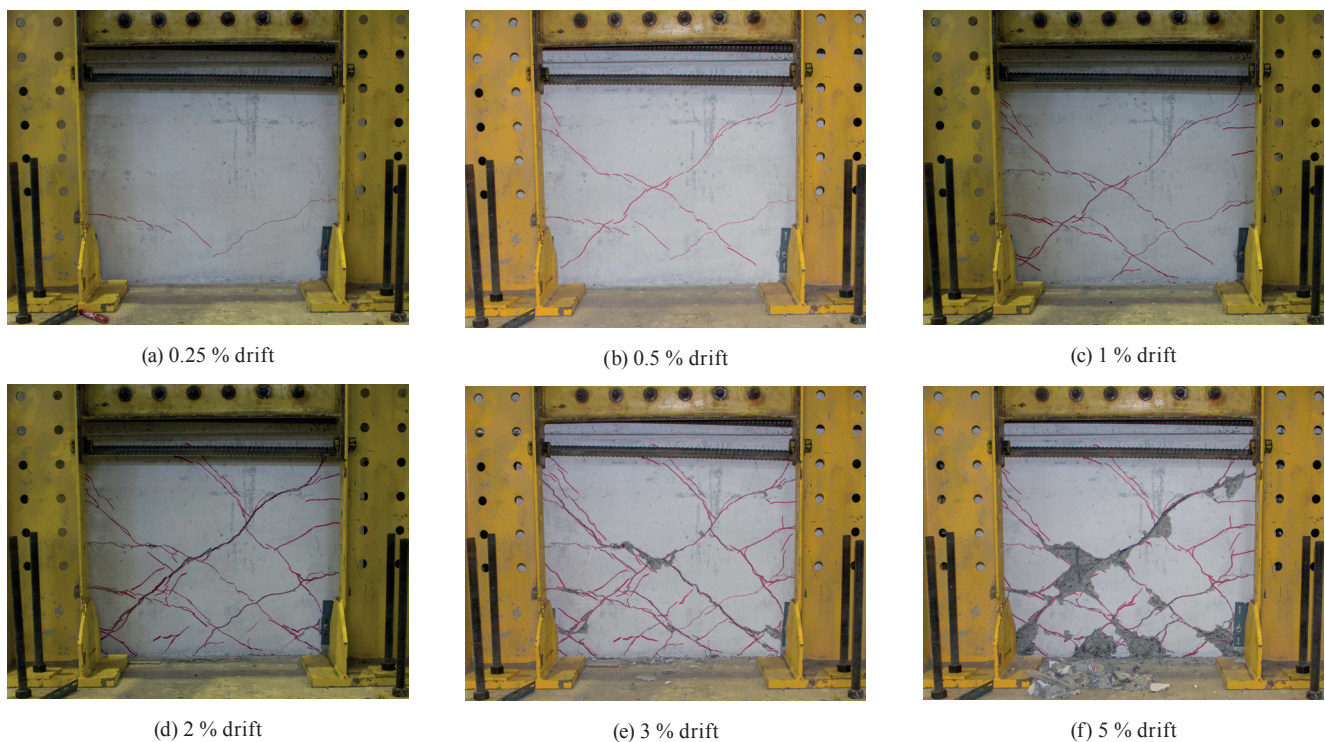

| (a) 0.25 % drift | (b) 0.5 % drift | (c) 1 % drift |
| (d) 2 % drift | (e) 3 % drift | (f) 5 % drift |

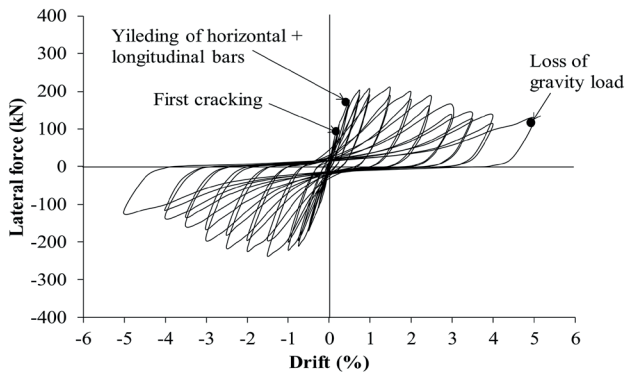**Fig. 7** Propagation of damage with drift increments specimen SW2

Fig. 8 Lateral force – Top drift relationship specimen SW2

main cracks continued to grow and caused the final failure of the specimen SW2. In the absence of axial compression load, diagonal cracks remained open when the applied lateral drift reached the zero level during the unloading phase and caused significant residual drift, as presented in Fig. 8. A significant shear slip was observed along the shear plane of the main crack, causing large pinched loops. The lateral strength degradation in the case of the SW2 specimen was more gradual and smoother than the SW1 specimen. The test was stopped at 5 % drift when the specimen SW2 was not able to carry the applied axial load. A peak shear stress of $0.4\sqrt{f_c'}$ was observed.

2.6 Components of lateral deformation

The extensive instrumentation was used to determine the contribution of each component of lateral deformation of the RC wall specimens. The total lateral deformation of an RC wall is comprised of the flexure, shear, rocking deformation, and shear slip components of lateral deformation.

2.6.1 Calculation procedure

In order to determine the flexure deformation, the specimen was divided into three sections along the height of the wall, and LVDTs were installed to obtain the rotation of the specific sections using the Eq. (1), whereas, flexural deformation (U_f) was calculated using Eq. (2).:

$$\theta_f = \frac{\Delta_1 - \Delta_2}{L_w},\tag{1}$$

$$U_f = \sum_1^i \theta_f d_i,\tag{2}$$

where θ_f is the average rotation of the section, Δ_1 and Δ_2 are the relative displacement parameters to calculate the rotation of the specific section, d_i is the vertical distance from the center of the specific section to the top of the

wall and L_w is length of the section [17]. Fig. 9(a) and 9(b) explain the calculation procedures of flexure deformation and shear deformation, respectively. The shear deformation (U_s') was calculated using the LVDTs (as shown in Fig. 4(b)) in the "X" configuration [18] and employing the following equation:

$$U_s' = \frac{\sqrt{D_1^2 - h^2} - \sqrt{D_2^2 - h^2}}{2}.\tag{3}$$

The shear deformation obtained from Eq. (3) is effected by flexure deformation, which results in an overestimation of the shear deformation [17]. The incorrect value of shear deformation can be corrected by using Eq. (4) [18]:

$$U_s = U_s' + \left(\frac{1}{2} - \alpha\right)\varphi h,\tag{4}$$

where U_s is the corrected shear deformation, U_s' is the incorrect shear deformation, α is the centroid of the curvature distribution, φ is the rotation over the region of the "X" configuration, and the parameter h is shown in Fig. 9(b) [17]. The value of α was equal to 0.67, which is consistent with the previous research [19]. The rocking or rigid body deformation of the shear wall specimen was determined using two LVDTs attached to the face of the shear wall specimen (Fig. 4(b)). The calculation procedure is explained in Fig. 9(c). Eq. (5) was used to calculate the rigid body deformation of the shear wall specimen:

$$U_r = \left(\frac{\Delta_1 - \Delta_2}{L_w}\right)H,\tag{5}$$

where U_r is the rigid body deformation, H is the total height of the shear wall, and Δ_1 and Δ_2 are the relative displacement parameters used to calculate the rotation at the
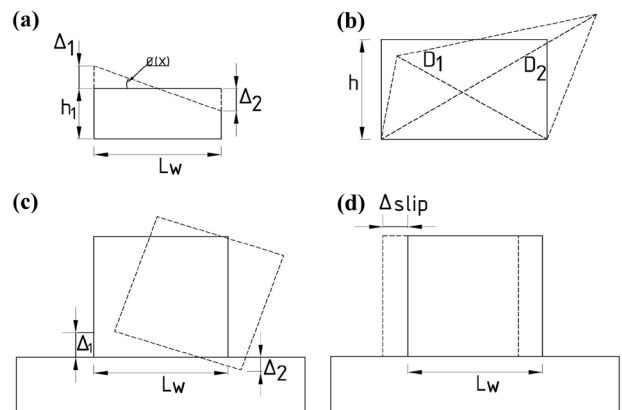

Fig. 9 Calculation of lateral deformation (a) Flexure (b) Shear (c) Rigid body/rocking (d) Shear slip

bottom of the specimen [17]. The shear slip deformation mode is presented in Fig. 9(d) which was obtained directly from the LVDT (i.e., F_s in Fig. 4(b)) installed at the interface of the base block and the RC wall specimen.

2.6.2 Respective contribution of lateral deformation components

Fig. 10 shows the contribution of each lateral deformation component for the specimen SW1. The shear deformation component exhibited the highest contribution (approximately 77 %) to the total lateral deformation. The shear slip deformation showed the lowest contribution (approximately 10 %) to the total lateral deformation, which is quite understandable because it is difficult for the RC wall specimen to slip due to high axial compression load. For the same reason, no pinching was noticed in the hysteretic response of the specimen SW1. The flexure deformation contributed approximately 20 % of the total deformation. It is important to note that as the shear deformation progressed into non-linear behavior, the flexure deformation also progressed into a non-linear response. This demonstrates the strong interaction between the flexure and the shear response, as explained earlier. In the available computer programs, a non-linear flexure and shear

response is typically modeled separately, which requires careful assessment of the interaction effects. The effects of the flexure-shear interaction in computer modeling are discussed in the following sections. The rocking deformation contributed approximately 8 % of the total deformation. The sum of the deformation components was slightly higher than the total lateral deformation measured at the top of the wall specimen, which might be due to an instrumental error. It is important to emphasize here that it is hard to disintegrate flexure and rigid body deformation components. Apart from the instrumentation error, another reason of this slight overestimation could be the spillover of the rigid body deformation to the flexural deformation.

Fig. 11 presents the contribution of each lateral deformation component for the specimen SW2. The shear deformation and shear slip deformation exhibited approximately the same contributions. The contribution of the shear slip to the total deformation was approximately 38 %, whereas the shear deformation contribution was approximately 39 %. The high shear slip deformation was attributed to significant slippage of the shear cracks. In the absence of the axial compression, the shear planes can easily slip along the direction of the principle compression stresses. Due to the high shear slip, the hysteretic
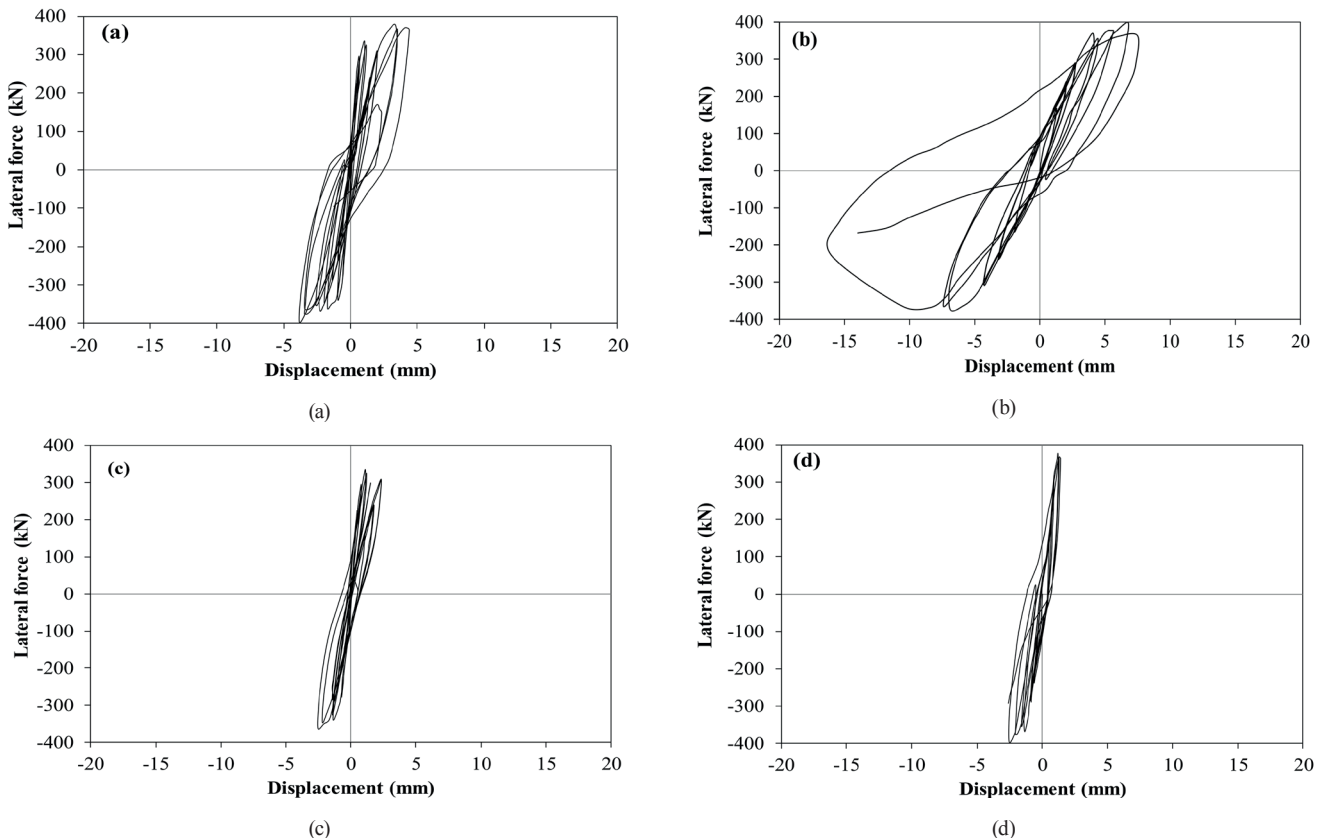

Fig. 10 Components of lateral deformation of SW1 (a) Flexure (b) Shear (c) Rigid body/rocking (d) Shear slip
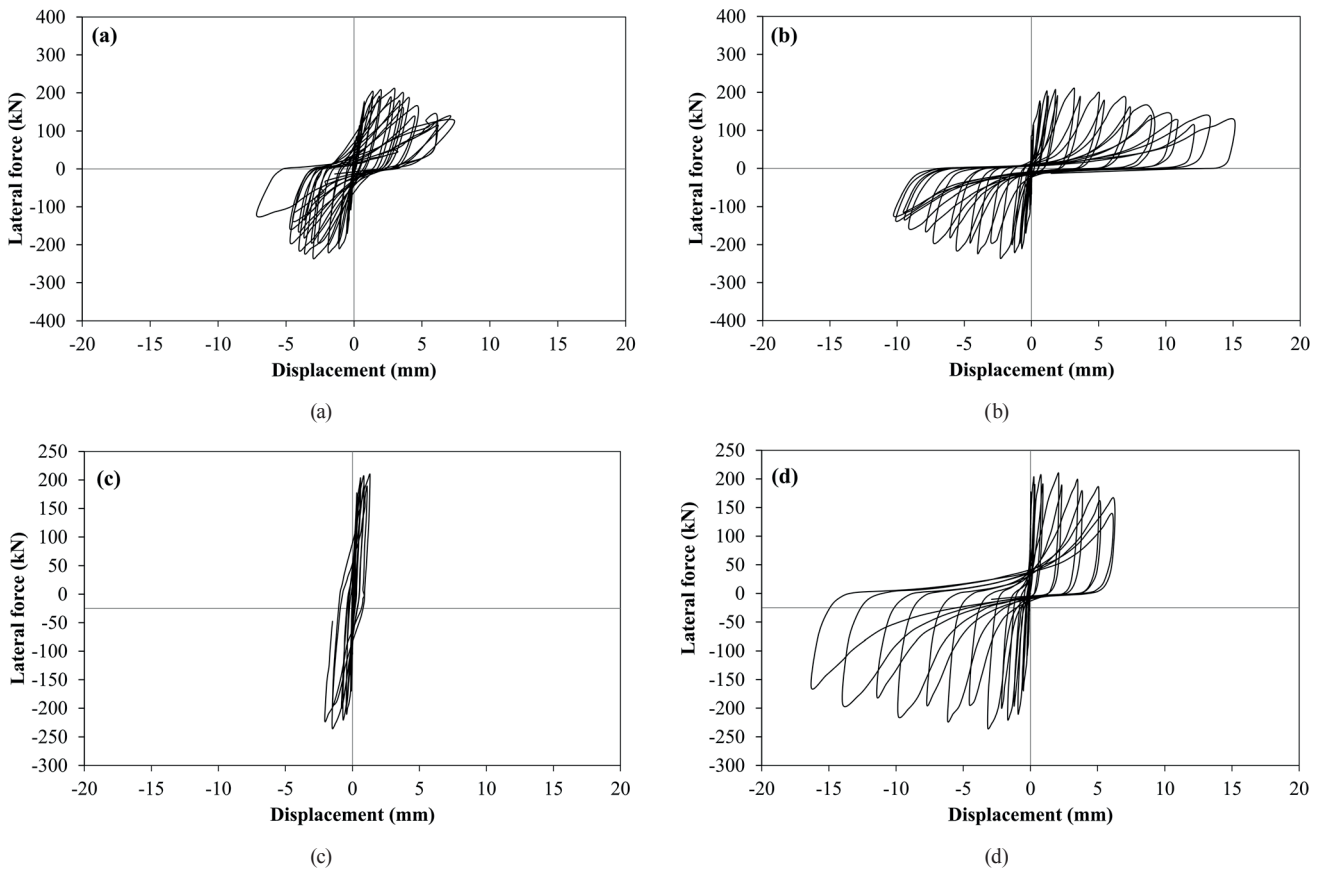
Fig. 11 Components of lateral deformation of SW2 (a) Flexure (b) Shear (c) Rigid body/rocking (d) Shear slip

responses exhibited large pinching loops in the case of the specimen SW2. Similar to the results of the specimen SW1, a strong interaction between the non-linear flexure and the shear responses was observed in the case of the specimen SW2. The flexure deformation contribution was approximately 16 % of the total deformation. The rocking deformation showed the lowest contribution (approximately 4 %) to the total deformation. The sum of the deformation components was roughly equal to the total lateral deformation measured at the top of the wall specimen.

2.6.3 Comparison of SW1 (10 % axial load) and SW2 (0 % axial load)

A brief comparison was made between the specimens SW1 and SW2 to determine the influence of the axial load on the shear capacity and deformation. One notable difference in both tested walls was the difference in shear capacity. The shear capacity of the specimen SW1 was 70 % more than that of the specimen SW2. The reason for this higher shear strength under axial compression can be explained by the crack angle of the specimens SW1 and SW2. Following the truss model with diagonals inclined at an angle of θ, the shear stress contribution of the horizontal reinforcement

can be predicted as $V_c + \rho_h f_y \cot\theta$, where ρ_h is the reinforcement ratio of the horizontal reinforcement, f_y is the yield strength of the horizontal reinforcement and V_c is the concrete contribution to the shear strength, which is approximately proportional to the $\sqrt{f_c'}$. Fig. 12 depicts the angle of the main crack in both the SW1 and SW2 specimens. It can be observed that the angle of strut in the case of the specimen SW1 was less than the angle of strut in the case of the specimen SW2, which leads to an increase in the shear strength of the SW1 specimen. The angle of strut (i.e., the angle of the diagonal compressive stresses) depends on the longitudinal strain in the web of RC walls [10]. The longitudinal strain decreased under the effect of the axial load or pre-stressing, which in turn decreased the angle of strut and thus increased the shear strength.

Fig. 13 presents the reversed cyclic force deformation response of the specimens SW1 and SW2. The shear strength, calculated by both equations of ACI 318-11 [7] is also plotted in Fig. 13. The shear strength equation of ACI 318-11 Chapter 21 [7], underpredicts the shear strength of the specimen SW1 by approximately 23 % due to the laxity of the beneficial effect of the axial load on the shear strength. On the other hand, the shear strength equation
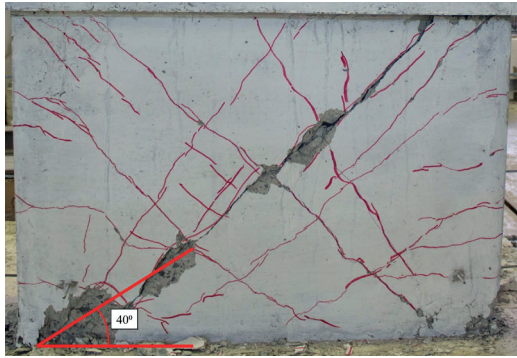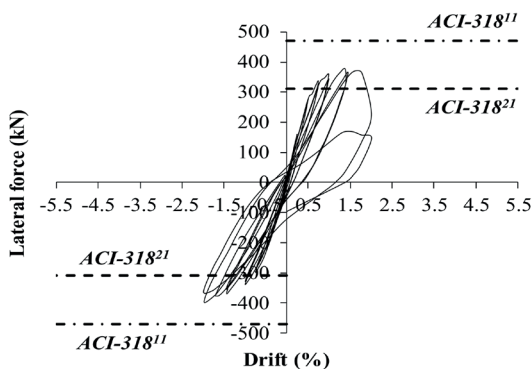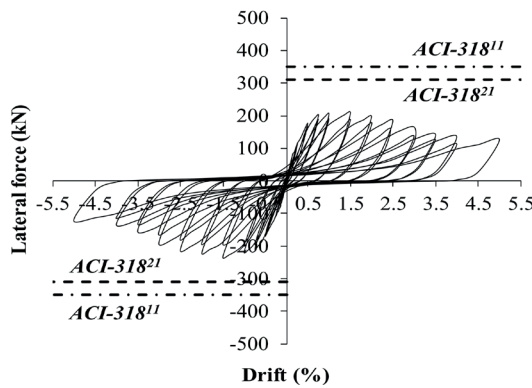
(a)
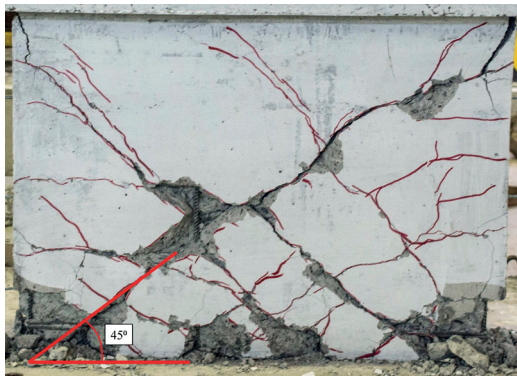
(b)

**Fig. 12** Comparison of cracks pattern (a) SW1 (b) SW2


(a)

(b)

Fig. 13 Comparison of force-drift (a) SW1 (b) SW2

of ACI 318-11 [7] from Chapter 21 overpredicts the shear strength of the specimen SW2 by a margin of 21 %. The shear strength equation of ACI 318-11, Chapter 11 [7], over-predicts the shear strength of SW1 and SW2 by approximately 20 % and 38 %, respectively. The reversed cyclic load-deformation response was also strikingly different for both specimens. The specimen SW1 was able to withstand the axial load up to a 2 % drift, whereas the specimen SW2 was able to develop large pinching loops up to a 5 % drift. Due to the axial load in the case of specimen SW1, cracks closed when the applied lateral drift reached the zero level during the unloading phase. In the case of the specimen SW2, the cracks continued to widen with the increase and decrease of the lateral drifts.

Another important finding is the effect of the axial load on the yield shear strain. Fig. 14 presents a comparison of the shear strain for the specimens SW1 and SW2. It is interesting to note that the presence of the axial load increased the yield shear strain in the specimen SW1 up to 3.15 times of that observed in the specimen SW2. It is very important to know when the strength is going to drop in the case of shear failure. The sharp degradation of the lateral strength was observed in the case of the specimen SW1, with a small ductility of 1.64 ($\mu = \Delta_{ult}/\Delta_y = 0.012/0.0073$), whereas in the case of the specimen SW2, a more gradual
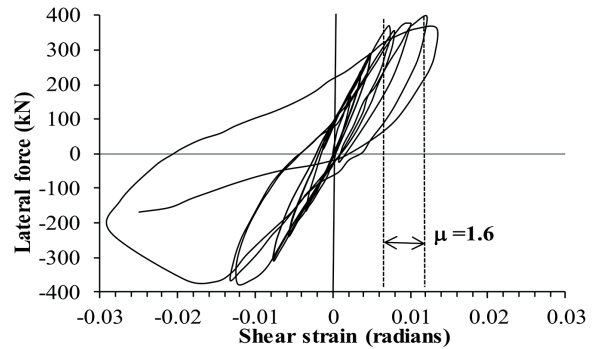
(a)
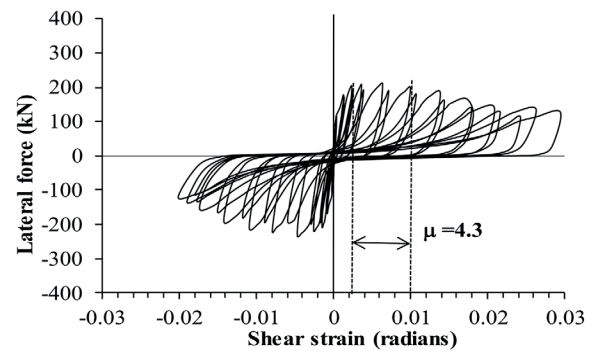
(b)

Fig. 14 Comparison of shear strain (a) SW1 (b) SW2

and smooth strength degradation was observed. A ductility factor of 4.3 was observed in the case of the specimen SW2, i.e., without any axial load.

2.7 Comparison with performance-based design codes
This section presents the comparison of effective flexure and shear rigidity with recommendations of ASCE-41-06 [12] and FEMA-356 [13]. The backbone curves for all the specimens are also constructed by following the recommendations of ASCE-41-06 [12], including supplement #1 [20], and FEMA-356 [13]. Results of constructed backbone curves are compared with the experimental results.

2.7.1 Effective flexure and shear rigidities
Effective flexure and shear stiffness are important parameters for the RC shear wall building to perform linear and non-linear analysis. ASCE-41 -Supplement #1 [20] and FEMA-356 [13] recommend a value $0.5E_cI_g$ for the cracked RC walls. FEMA-356 [13] also suggests a value of $0.8E_cI_g$ for un-cracked RC walls. ASCE-41-Supplement #1 [20] and FEMA-356 [13] suggest a value of $0.4E_cA_w$ for cracked RC walls. FEMA-356 [13] also suggests the same value (i.e., $0.4E_cA_w$) for un-cracked RC walls. The effective secant flexure values of the tested RC walls specimen were determined based on the lateral stiffness of the cantilever RC walls as:

$$F = K_f\Delta_f \quad \text{where} \quad K_f = \frac{3E_cI_{eff}}{h_w^3}. \tag{6}$$

Therefore, secant flexural stiffness normalized by the concrete gross section flexural stiffness was determined as:

$$\frac{I_{eff}}{I_g} = \frac{E_cI_{eff}}{E_cI_g} = \frac{K_fh_w^3}{3E_cI_g} = \frac{h_w^3}{3E_cI_g}\left(\frac{F}{\Delta_f}\right), \tag{7}$$

where F is the lateral force, Δ_f is the flexure displacement, h_w is the height of RC walls and E_c is the Young's modulus of concrete determined using ACI 318-11 [7] requirements. Similarly, the secant shear stiffness normalized by E_cA_w can be determined as follows:

$$\frac{GA_{eff}}{E_cA_W} = \frac{F/\gamma_s}{E_cA_W} = \frac{h_w}{E_cA_W}\left(\frac{F}{\Delta_s}\right), \tag{8}$$

where F is the lateral load, γ_s is the shear strain, Δ_s is the shear displacement at the top of the wall and A_w is the wall cross-section area.

Fig. 15 presents the results of effective secant flexure stiffness values versus drift ratios obtained from the experimental results. Results indicate that un-cracked flexure

stiffness value was approximately $0.5E_cI_g$ which was much lower than the recommended value of FEMA-356 [13] (i.e., $0.8E_cI_g$). The cracked flexure stiffness was approximately $0.3E_cI_g$ which was also lower than the value suggested by ASCE-41-Supplement #1 [20] and FEMA-356 [13] (i.e., $0.5E_cI_g$).

Fig. 16 shows the result of the experimental results of effective shear stiffness plotted against the drift ratios. It can be noticed that the effective un-cracked shear stiffness was approximately $0.22E_cA_w$, whereas cracked effective shear stiffness was approximately $0.08E_cA_w$. These values were much lower than that suggested by the recommendations of both the documents i.e., ASCE-41-Supplement #1 [20] and FEMA-356 [13].

2.7.2 Load- deformation backbone curves comparison
The non-linear backbone curves were determined by following the recommendations of ASCE-41-Supplement #1 [20] and FEMA-356 [13]. Fig. 17 presents the comparison of experimental results with the derived backbone curves based on the seismic acceptance criteria provided in ACSE-41-Supplement #1 [20] and FEMA-356 [13]. The cracking and ultimate shear strength of the specimens SW1 and SW2 were calculated following the recommendations of ACI 318-11 [7]. As mentioned earlier, ACI 318-11 [7]
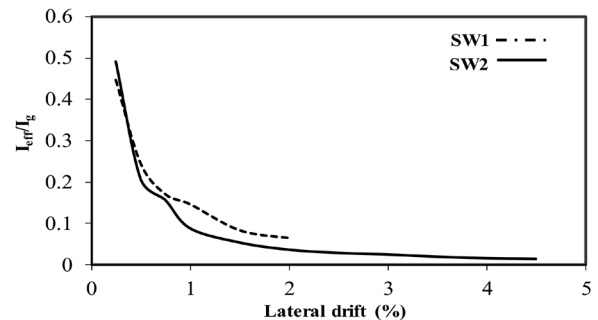
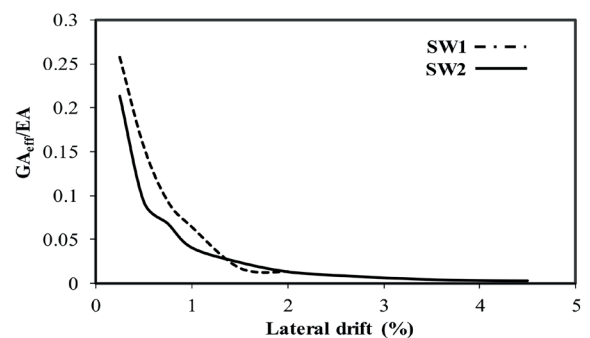**Fig. 15** Effective flexure secant stiffness values obtained from experimental results

Fig. 16 Effective shear secant stiffness values obtained from experimental results
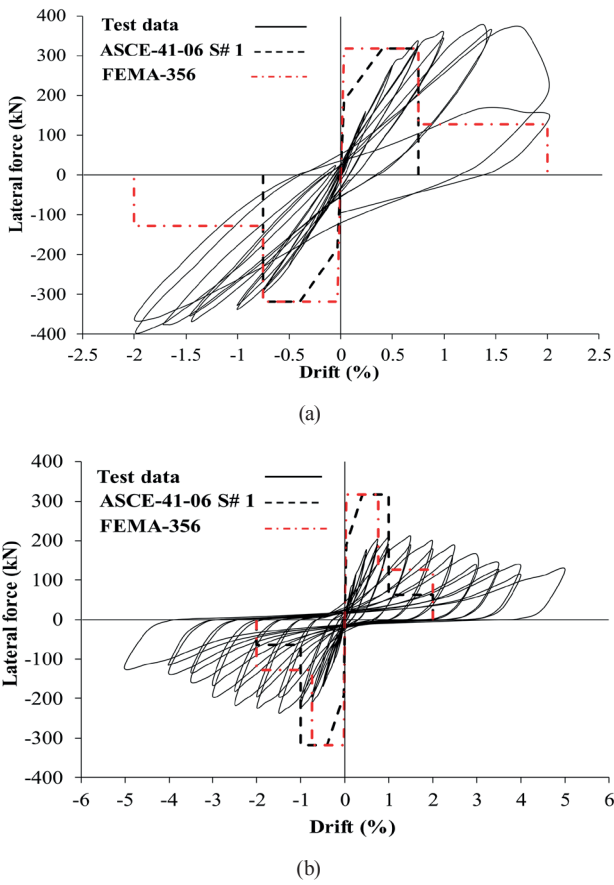
Fig. 17 Comparison of lateral force –top drift relationship with ASCE-41-06-Supplement #1 and FEMA-356-2000 (a) SW1 (b) SW2

underestimates the shear strength of the specimen SW1, since the influence of the axial load is not considered, and overestimates the shear strength of the specimen SW2. The yield and ultimate deformation were underestimated by both ASCE-41-Supplement #1 [20] and FEMA-356 [13] for the specimen SW1 and SW2.

The level of deformation corresponding to the drop in shear strength is greatly important for collapse prevention of the structural members. The collapse prevention deformation limit is also important for the existing RC walls so that the amount of required confinement can be calculated and consequently the overall cost of rehabilitation. The presence of axial load decreased the ductility of shear dominated RC walls (i.e., SW1). Similar results were obtained by Massone [21] for RC walls with and without axial load. Such variation in shear ductility due to axial load was not included in the ASCE-41-06 [12] and FEMA-356 [13]. In ASCE-41-06-Supplement #1 [20], a decrease in the ductility of shear-response dominated RC wall under axial load was included based on the limited data [21]. The comparison of collapse prevention limit of ASCE-41-Supplement #1 [20] and FEMA-356 [13] with

the experimental results of shear-response dominated RC walls tested in the current study show that both the code provisions (i.e., ASCE-41-06-Supplement #1 [20] and FEMA-356 [13]) underestimate the ductility of the SW1 and SW2.

3 Numerical study
Three different types of computer modeling approaches were adopted in this study. The first approach is the conventional fiber modeling in which the shear response was modeled as linear elastic. The second approach is also a fiber modeling approach, but shear response of the RC wall specimens was modeled as nonlinear, while the third one was a rigorous FE modeling approach including axial-flexure-shear interaction. This study enables us to determine the effect of computer modeling to predict the nonlinear response of RC walls and helps to select the most suitable modeling approach for the nonlinear seismic response analysis of RC walls.

3.1 Fiber modeling of RC wall specimens
Three different RC properties were used to model the experimentally tested specimens. The employed web and boundary RC properties are presented in Table 1. The top beam and the base block were modeled using the elastic material properties because no damage was noticed in the test. The web of the RC wall specimens was divided into four horizontal layers while one layer was used to model the boundary region. Each layer contained 8 steel and 8 concrete vertical fibers. Suitable constitutive models were used to model the concrete and reinforcement behavior. For reinforcement, a tri-linear model was used, which can account for the strain hardening. It consisted of an initial linear-elastic response, a yield plateau, and a linear strain-hardening phase until the rupture. Mander's model [22] was used to model the behavior of confined and unconfined concrete. It should be noted that this model can account for axial-flexure interaction, but axial-flexure-shear interaction cannot be simulated by this model. The shear response was modeled as linear elastic, that was independent of the axial-flexure response behavior. Same reversed cyclic loading was applied as used in the experiment.

Fig. 18 shows the comparison of force-deformation response obtained from the conventional fiber modeling approach and the one obtained from the experimental results of the specimen SW1. As can be observed, the fiber model significantly overestimated the shear capacity of the specimen SW1. The reason for this overestimation of shear
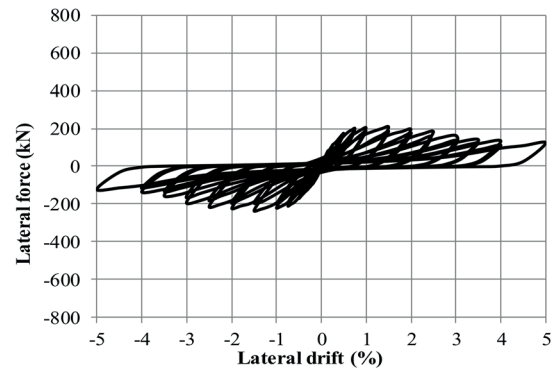
Fig. 18 Comparison of results of SW1 (a) Experimental (b) Numerical
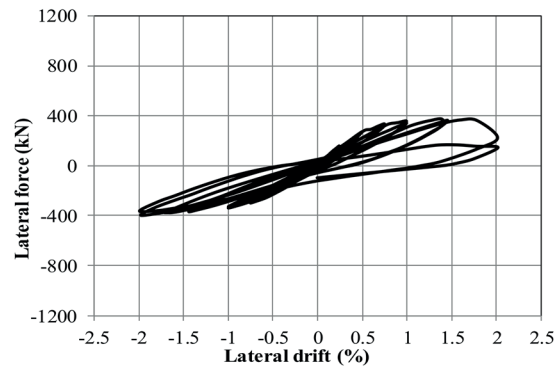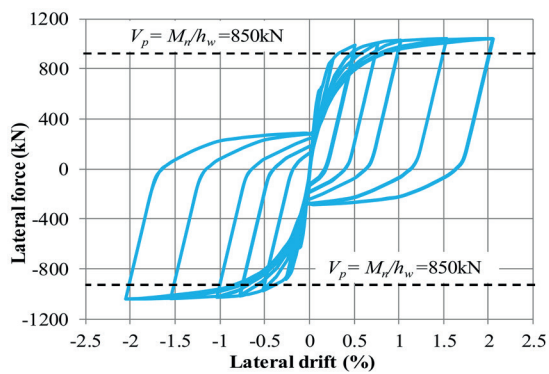
Fig. 19 Comparison of results of SW2 (a) Experimental (b) Numerical

capacity is obvious as the shear response was modeled as linear elastic and there was no limit on the shear capacity; therefore, shear demand can only be saturated once the flexural capacity is achieved. Shear load against the nominal flexural capacity is also shown in Fig. 18. Similarly, for RC wall specimen SW2, shear capacity was greatly overestimated as shown in Fig. 19. The reason for the overestimation in shear capacity is same as explained in the case of SW1. It should be noted that the shear capacity predicted by the fiber model for the specimen SW2 was lower than the shear capacity of SW1 due to difference in the nominal moment capacity under axial load effect.

3.2 Numerical modeling of RC wall specimen including nonlinear shear response

In the previous section, it is discussed that the conventional fiber modeling approach failed to predict the shear capacity of the specimens SW1 and SW2. In this section, the nonlinear shear response was considered by following the recommendations of the performance-based code procedure. Similar fiber modeling approach was adopted in this section, as explained earlier; however, the shear response was modeled as tri-linear curve according to the guidelines provided in ASCE-41-06 [12]. Fig. 20 shows the
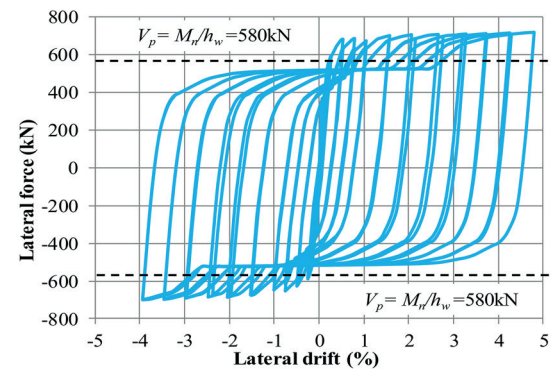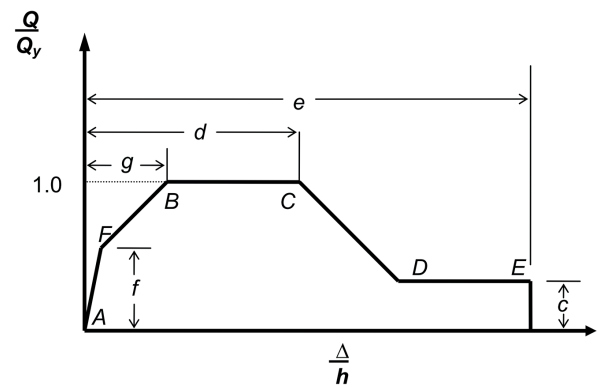

Fig. 20 Modeling of shear response in RC walls backbone curve-ASCE-41-06 [12]

backbone curve used for the nonlinear shear response. The values of deformation parameters (g, d, c) in Fig. 20 were obtained from the Table 19 of Chapter 6 provided in the code ASCE-41-06 [12], while the cracking and yield shear strengths were calculated from the code ACI 318-11 [7]. The shear strength of RC wall specimens was calculated from Eq. (9), as recommended by the ACI 318-11 [7], Chapter 21.

$$V_n = A_{cv} \left(\alpha_c \sqrt{f_c'} + \rho_h f_y \right), \tag{9}$$

where V_n is the nominal shear strength, A_{cv} is gross web area, α_c is 3.0 for $h_w/l_w \leq 1.5$, 2.0 for $h_w/l_w \geq 2.0$ and varies linearly between 3.0 and 2.0 for h_w/l_w between 1.5 and 2.0, ρ_h is the horizontal reinforcement ratio and f_y is the yield strength of the horizontal reinforcement. The hysteretic response of shear response was modeled in Perform3D by following the Modified Takeda's model. It should be noted that although the shear response was modeled as nonlinear, the interaction between axial, flexure and the shear response could not be considered for this type of modeling approach. Other modeling assumptions for the RC wall specimens were same as presented in the previous section.

Fig. 21 displays the comparison of force-deformation response obtained from the numerical model including nonlinear shear response and the one obtained from the experimentation of the specimen SW1. Although the numerical model was successfully able to predict the shear failure, it underestimated the shear capacity of the specimen SW1. As observed in the experimental results, although the shear capacity of the specimen SW1 was significantly increased under axial compression load, the numerical model failed to take into account this beneficial effect of axial compression. Moreover, the computer model overestimated the

initial stiffness. Fig. 22 shows the comparison of force-deformation for the specimen SW2 obtained from the numerical model and the experiment. The numerical model overestimated the shear capacity for the specimen SW2. The degradation in the force-deformation was predicted, but the numerical model underestimated the ductility. The hysteretic response was also significantly different from the one observed in the experiment.

3.3 Axial-Flexure-Shear interaction modeling of RC wall specimens
From the experimental results presented earlier, it is clear that there is a strong relationship between the flexural and shear responses. Another important outcome of the experimental study is that the shear strength was significantly influenced by the axial compression load. In this section, the VecTor2 [23] computer program based on the Modified Compression Field Theory (MCFT) [14] was used to capture axial-flexure-shear interaction, as observed in experimental results. In the FE model, the Hogdnestad parabolic model [24] was used for the pre-peak response of concrete in compression, while Modified Park-Kent model [25] was used for the post-peak response of concrete in compression.
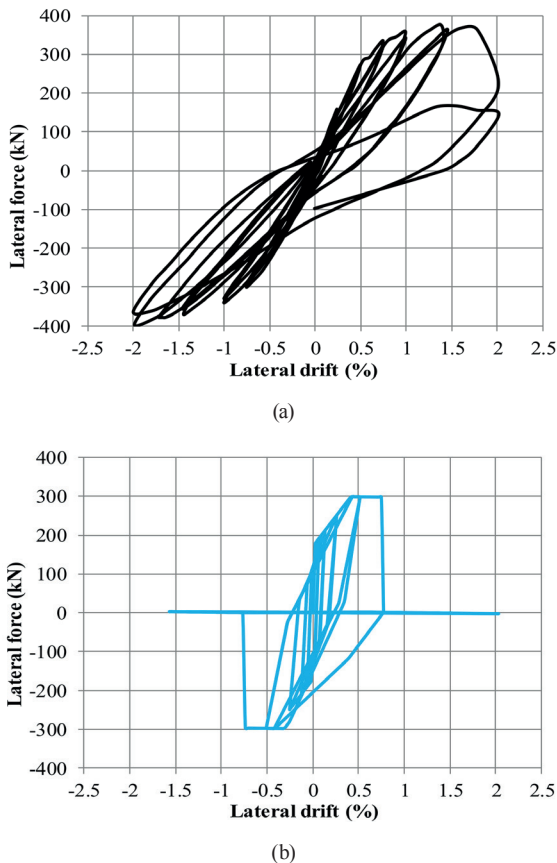

(a)

(b)

Fig. 21 Comparison of results of SW1 (a) Experimental (b) Numerical
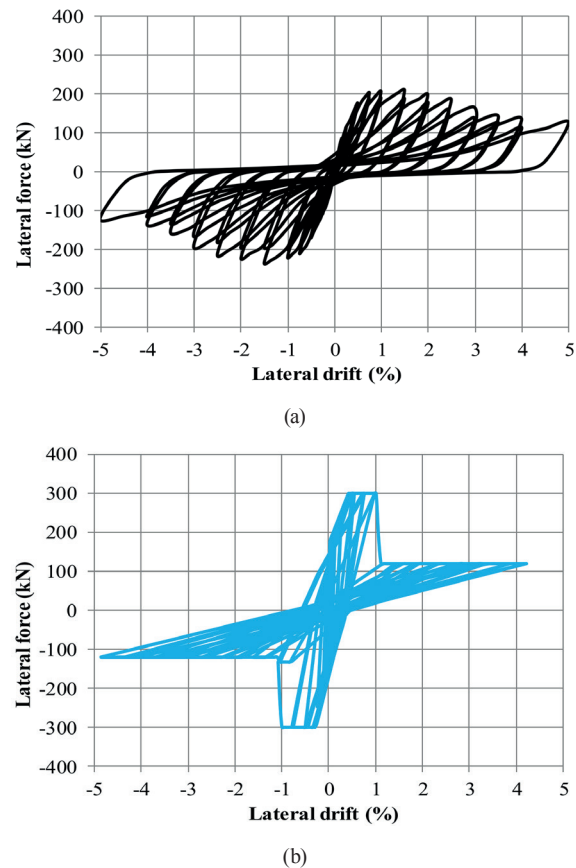

(a)

(b)

Fig. 22 Comparison of results of SW2 (a) Experimental (b) Numerical

The hysteretic model proposed by Palermo and Vecchio [26] was used for concrete hysteresis. Slip distortion was considered using the Vecchio and Lai [27] model. For reinforcement, a tri-linear model was used, which can account for the strain-hardening. It consists of an initial linear-elastic response, a yield plateau, and a linear strain-hardening phase until rupture. The hysteretic response of the reinforcement was modeled using the Seckin hysteresis model [28], which can incorporate the Bausichinger effect. The tension stiffening effect was also considered for the FE analysis according to the model proposed by Seong-Cheol Lee [29]. RC wall specimens were modeled in the VecTor2 [23] computer program using 2D plane stress elements. Three different RC properties were used to model the experimentally tested specimens. The web and boundary RC concrete properties were provided, as shown in Table 1. The top beam and the base block were modeled using the elastic material properties because no damage was observed in the test. The mesh size was selected without compromising the accuracy. Both specimens SW1 and SW2 were modeled with same properties, except for a difference in the axial load application.

Fig. 23 presents the comparison of the VecTor2 [23] and the experimental load-deformation relationship of the specimen SW1. An excellent prediction of the shear strength was observed in the numerical results. The shear strength started degrading approximately at the same stage as observed in the experiment. The initial stiffness predicted by VecTor2 [23] was slightly higher than the observed value in the experiment, which was maybe due to the ideal boundary conditions assumed in the FE model, making the FE model stiffer. The hysteretic response matched reasonably well with the experimental results.

The comparison of the numerical and experimental results for the specimen SW2 is presented in Fig. 23. Similar to the specimen SW1, an excellent agreement was found in the shear strength results, but the maximum deformation was underestimated by the FE model. The numerical results predicted large pinched loops, as observed in the experimental results for the specimen SW2. The initial stiffness was slightly overestimated by the FE model. Nevertheless, the FE model in the VecTor2 [23] software was able to predict the shear strength under the combined effect of the axial-flexure-shear interaction for both SW1 and SW2 specimens, with significant accuracy.
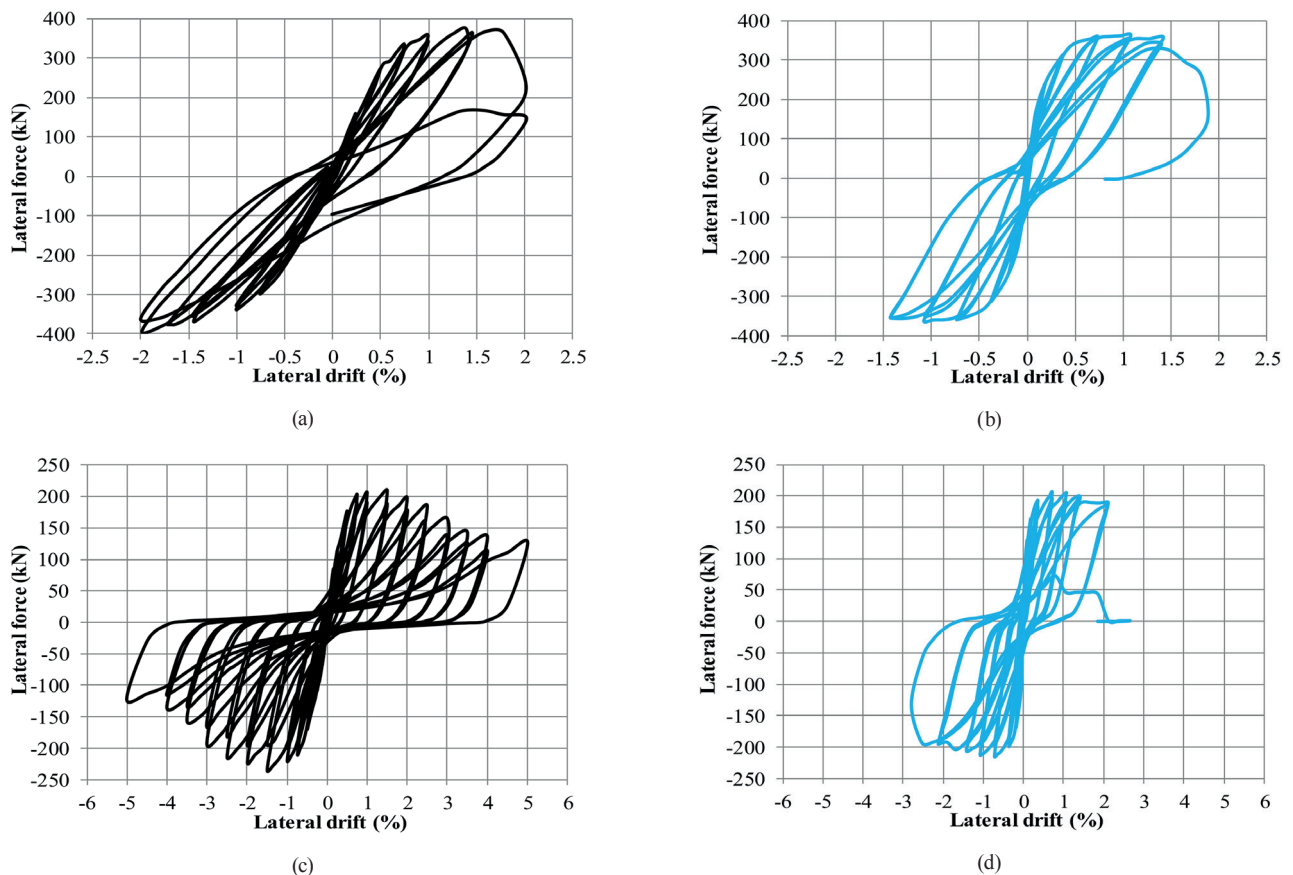

Fig. 23 Comparison of results (a) Experimental SW1 (b) Numerical SW1 (c) Experimental SW2 (d) Numerical SW2

4 Conclusions

An experimental program was designed to investigate the effect of axial compression on the shear strength of RC walls. Two identical RC wall specimens were tested, one under the axial compression and one without axial loading. Various numerical modeling approaches were studied, with different level of sophistication, to capture the nonlinear response. Following conclusions can be drawn from the current study:

This study highlights the effect of axial compression on the shear strength and ductility of RC walls. One important conclusion of this experimental study is that while calculating the shear strength of the RC walls, the beneficial effect of the axial load should not be ignored. There is a need to use a reliable method of shear strength calculations of the RC walls. In the current study, it was found that the level of axial load is related to available ductility capacity of RC shear walls. One critical observation made in this regard is that there is relatively lower ductility available in the shear-dominated RC walls under the axial compression. Therefore, when a designer wants to promote a flexure failure in the RC walls, the importance of an accurate estimation of the shear strength/shear deformations responses should be considered. This study concludes that the ductility of the shear strain decreases with the application of axial load. Therefore, for the RC walls under high axial compression, shear yielding should be avoided. Although significant ductility in shear is observed in the case of the RC walls under a little or no axial compression, further studies are needed to confirm this observation. The ACI 318-11 [7] underpredicts the shear strength of the specimen under axial compression (SW1) and overpredicts the shear strength of the specimen for the RC walls

without axial load application (SW2). The ACI 318-11 [7] overpredicts the shear strength of both specimens with and without axial compression.

The comparison of flexure and shear rigidities with ASCE-41-Supplement #1 [20] and FEMA-356 [13] shows that both the codes greatly underestimate the un-cracked as well as the cracked effective flexure and shear rigidities, which needs revision based on the recent experimental data, such as provided in the current study. Moreover, the load-deformation backbones provided in both the codes are not a true representation of the actual response of shear dominated RC walls, especially under the axial load effect.

In the current study, it was found that the axial-flexure-shear interaction needs to be incorporated for accurate numerical modeling of the shear dominated RC walls. The conventionally adopted fiber modeling technique by considering linear elastic shear response behavior would not be a suitable choice for shear response dominated RC walls. One the other hand, the combination of non-linear shear response integrated with the fiber modeling of RC walls could also result in the erroneous prediction of shear strength and lateral force-deformation behavior. The FE model, based on MCFT, found to be capable of simulating the axial-flexure-shear interaction, as observed in the experimental study whereas, the fiber modeling approaches, with or without nonlinear shear response modeling, failed to predict the key experimental observations. The FE model, based on the MCFT theory available in the VecTor2 software platform, is capable of accurately calculating the shear strength of the RC walls but underestimates the deformation.

References

[1] Luu, H., Ghorbanirenani, I., Léger, P., Tremblay, R. "Numerical Modeling of Slender Reinforced Concrete Shear Wall Shaking Table Tests Under High-Frequency Ground Motions", Journal of Earthquake Engineering, 17(4), pp. 517–542, 2013.
https://doi.org/10.1080/13632469.2013.767759

[2] Munir, A., Warnitchai, P. "The cause of unproportionately large higher mode contributions in the inelastic seismic responses of high-rise core-wall buildings", Earthquake Engineering & Structural Dynamics, 41(15), pp. 2195–2214, 2012.
https://doi.org/10.1002/eqe.2182

[3] Priestley, M. J. N., Amaris, A. D. "Dynamic Amplification of Seismic Moments and Shear Forces in Cantilever Walls", IUSS Press, Pavia, Italy, 2002.

[4] Rad, B. R., Adebar, P. "Dynamic shear amplification in high-rise concrete walls: effect of multiple flexural hinges and shear cracking", presented at Proceedings of the 14th World Conference on Earthquake Engineering, Beijing, China, Oct. 12–17, 2008.

[5] Paulay, T., Priestley, M. J. N. "Seismic Design of Reinforced Concrete and Masonry Buildings", Wiley, New York, NY, USA, 1992.
https://doi.org/10.1002/9780470172841

[6] Aktan, A. E., Bertero, V. V. "Seismic Response of R/C Frame-Wall Structures", Journal of Structural Engineering, 110(8), pp. 1803–1821, 1984.
https://doi.org/10.1061/(ASCE)0733-9445(1984)110:8(1803)

[7] American Concrete Institute "ACI 318-11, Building Code Requirements for Structural Concrete and Commentary", ACI, Farmington Hills, MI, USA, 2011.

[8]   Herrera, L., Tran, T. A., Wallace, J. W. "Lateral load behavior and modeling of low-rise RC walls for performance-based design", presented at Society for Advancement of Hispanics/Chicanos and Native Americans in Science National Conference, San Jose, CA, USA, Oct. 27–30, 2011.

[9]   Gulec, C. K., Whittaker, A. S., Stojadinovic, B. "Peak Shear Strength of Squat Reinforced Concrete Walls with Boundary Barbells or Flanges", ACI Structural Journal, 106(3), pp. 368–377, 2009.
https://doi.org/10.14359/56501

[10] Bentz, E. C., Vecchio, F. J., Collins, M. P. "Simplified Modified Compression Field Theory for Calculating Shear Strength of Reinforced Concrete Elements", ACI Structural Journal, 103(4), pp. 614–624, 2006.
https://doi.org/10.14359/16438

[11] American Society of Civil Engineers "ASCE 43-05, Seismic Design Criteria for Structures, Systems, and Components in Nuclear Facilities", ASCE, Reston, VA, USA, 2005.
https://doi.org/10.1061/9780784407622

[12] American Society of Civil Engineers "ASCE/SEI 41-06, Seismic Rehabilitation of Existing Buildings", ASCE, Reston, VA, USA, 2007.
https://doi.org/10.1061/9780784408841

[13] Federal Emergency Management Agency "FEMA 356-Prestandard and Commentary for the Seismic Rehabilitation of Buildings", FEMA, Washington, DC, USA, 2000.

[14] Vecchio, F. "The response of reinforced concrete to in-plane shear and normal stresses", Publication, University of Toronto, Toronto, ON, Canada, 1982.

[15] Mehmood, T., Rodsin, K., Warnitchai, P., Kolozvari, K. "Investigating the vulnerability of nonductile reinforced concrete columns in moderate seismic regions to gravity load collapse", The Structural Design of Tall and Special Buildings, 28(4), Article number: e1578, 2019.
https://doi.org/10.1002/tal.1578

[16] Lopes, M. S. "Experimental shear-dominated response of RC walls: Part I: Objectives, methodology and results", Engineering Structures, 23(3), pp. 229–239, 2001.
https://doi.org/10.1016/S0141-0296(00)00041-9

[17] Mehmood, T. "Investigation of nonlinear seismic response of high-rise RC wall structures using modal decomposition technique", PhD Dissertation, Asian Institute of Technology, 2015.

[18] Massone, L. M., Orakcal, K., Wallace, J. W. "Flexural and shear responses in slender RC shear walls", presented at 13th World Conference On Earthquake Engineering, Vancouver, BC, Canada, Aug. 1–6, 2004.

[19] Thomsen, J. H., Wallace, J. W. "Displacement-based design of RC structural walls: an experimental investigation of walls with rectangular and T-shaped cross-sections", Clarkson University, Potsdam, NY, USA, Rep. CU/CEE-95/06, 1995.

[20] Elwood, K. J., Matamoros, A. B., Wallace, J. W., Lehman, D. E., Heintz, J. A., Mitchell, A. D., Moore, M. A., Valley, M. T., Lowes, L. N., Comartin, C. D., Moehle, J. P. "Update to ASCE/SEI 41 Concrete Provisions", Earthquake Spectra, 23(3), pp. 493–523, 2007.
https://doi.org/10.1193/1.2757714

[21] Massone, L. M. "Strength prediction of squat structural walls via calibration of a shear–flexure interaction model", Engineering Structures, 32(4), pp. 922–932, 2010.
https://doi.org/10.1016/j.engstruct.2009.12.018

[22] Mander, J. B., Priestley, M. J. N., Park, R. "Theoretical Stress-Strain Model for Confined Concrete", Journal of Structural Engineering, 114(8), pp. 1804–1826, 1988.
https://doi.org/10.1061/(ASCE)0733-9445(1988)114:8(1804)

[23] Wong, P. S., Vecchio, F. J., Trommels, H. "VecTor2 & FormWorks User's Manual" [pdf] 2nd ed., VecTor Analysis Group, 2013. Available at: http://vectoranalysisgroup.com/user_manuals/manual1.pdf [Accessed: 05 May 2019]

[24] Popovics, S. "A numerical approach to the complete stress-strain curve of concrete", Cement and Concrete Research, 3(5), pp. 583–599, 1973.
https://doi.org/10.1016/0008-8846(73)90096-3

[25] Scott, B. D., Park, R., Priestley, M. J. N. "Stress-Strain Behavior of Concrete Confined by Overlapping Hoops at Low and High Strain Rates", ACI Journal Proceedings, 79(1), pp. 13–27, 1982.

[26] Palermo, D., Vecchio, F. J. "Behaviour and analysis of reinforced concrete walls subjected to reversed cyclic loading", University of Ottawa, Toronto, ON, Canada, Rep. 2002-01, 2002.

[27] Vecchio, F. J., Lai, D. "Crack Shear-Slip in Reinforced Concrete Elements", Journal of Advanced Concrete Technology, 2(3), pp. 289–300, 2004.
https://doi.org/10.3151/jact.2.289

[28] Seckin, M. "Hysteretic behaviour of cast-in-place exterior beam-column-slab subassemblies", PhD Dissertation, University of Toronto, 1981.

[29] Lee, S.-C., Cho, J.-Y., Vecchio, F. J. "Diverse Embedment Model for Steel Fiber-Reinforced Concrete in Tension: Model Verification", ACI Materials Journal, 108(5), pp. 526–535, 2011.
https://doi.org/10.14359/51683262